Journal of Nuclear Materials 377 (2008) 352–358

Contents lists available at ScienceDirect

Journal of Nuclear Materials

journal homepage: www.elsevier.com/locate/jnucmat

An indentation system for determination of viscoplastic stress–strain behavior of small metal volumes before and after irradiation

N. Huber [a,*], E. Tyulyukovskiy [b], H.-C. Schneider [b], R. Rolli [b], M. Weick [b]

[a] GKSS-Research Centre Geesthacht, Institute of Materials Research, Materials Mechanics, Max-Planck-Straße 1, 21502 Geesthacht, Germany
[b] Forschungszentrum Karlsruhe, Institute for Materials Research II, Postfach 3640, 76021 Karlsruhe, Germany

ARTICLE INFO

Article history:
Received 22 February 2006
Accepted 6 March 2008

ABSTRACT

The development of fusion materials for the first wall in future fusion reactors requires methods for the investigation of irradiation effects on the mechanical properties of materials which are only available in small volumes. Depth and force reading hardness measurement (or indentation) is one of the candidates that have the potential to extract valuable information on the stress–strain behavior of a material. A modified commercial indentation device installed in a hot cell of a fusion materials laboratory (FML) in combination with a neural network based analysis method allows identifying the material parameters of a unified viscoplasticity model with nonlinear isotropic and kinematic hardening from small metal specimens. By investigation of the same material before and after irradiation the method provides the possibility to separate irradiation effects on modulus, hardening and viscous behavior.

1. Introduction

Materials currently under investigation for future fusion reactors' first wall concepts are low activation ferritic-martensitic steels, e.g. the alloy Eurofer 97, as well as protective coatings of tungsten of several millimeters. These tungsten coatings fulfil the strong requirements regarding low activation and plasma compatibility due to low sputter rates on one hand and the temperature stability of the microstructure on the other hand. Both materials are object of extensive long term irradiation programs to study their mechanical behavior throughout irradiation at high doses.

Tungsten coatings of several millimeters in thickness can be produced by plasma spraying or CVD. Such coatings are of interest as a protection material for plasma facing first wall components made of Eurofer steel. The mechanical behavior of such tungsten coatings and its behavior after irradiation are totally unknown. Much better investigated is the mechanical behavior of Eurofer 97. Because only small volumes can be irradiated at high doses due to the limited volume in the available reactors, methods are generally required with which the mechanical properties of comparable small volumes can be tested. Currently available are small specimen tests for charpy-type impact and tensile testing [1–3]. These methods will be complemented by an indentation test described in this paper.

Advances in investigating the influence of irradiation on the hardening behavior of nuclear materials by means of indentation techniques have been made with the discovery of depth and force sensing indentation, which opened up new possibilities in characterizing small volumes [4]. Yamamoto et al. [5] developed a device for cyclic ball indentation test for small-sized specimens and analysed these data using the ABI technique (see e.g. [6]), which is widely used especially in reactor applications. Later they improved their analysis by modeling the small specimens using the finite element method [7]. Other researchers used micro, ultra-micro, or nano-indentation techniques to investigate the influence of helium co-implantation on ion-induced hardening of low activation ferritic steel [8], the hardening behavior of ion irradiated reduced activation ferritic/martensitic steels [9] the radiation hardening in Fe alloys under heavy ion irradiation [10], or the radiation and helium effects on the deformation behavior in ferrous alloys [11]. Beside such typical applications of indentation methods there were also attempts to estimate the fracture toughness transition curves of RPV steels by using ball indentation and tensile test data [12].

The quantities, which are continuously measured by depth and force sensing indentation systems are the force P and the indentation depth h as presented in Fig. 1. When using a spherical indenter of radius R the contact radius a is defined from the contact area under load and is not identical to the contact radius visible after removing the indenter, which is used for conventional hardness measurement. The contact radius a', which corresponds to the case where no pile up or sink in is present, can be calculated simply from the indenter radius and the indentation depth. For many methods proposed in literature the true contact radius a has to be determined indirectly from the available force–depth behavior. Some do only account correctly for sinking in, which is typically present for hard and highly elastic materials, as well as for softer materials with low strain hardening rate [4,13]. More sophisticated

* Corresponding author. Tel.: +49 4152/87 2500; fax: +49 4152/87 2534.
E-mail address: norbert.huber@gkss.de (N. Huber).

0022-3115/$ - see front matter © 2008 Elsevier B.V. All rights reserved.
doi:10.1016/j.jnucmat.2008.03.013

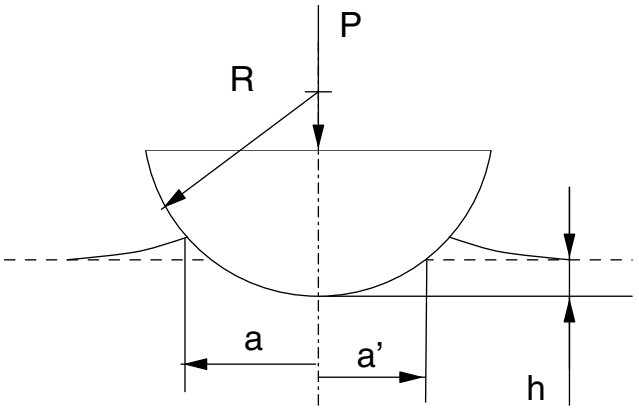

Fig. 1. Sketch and important variables of a spherical indent.

approaches for determining the pile up make use of finite element simulations and multiple partial unloadings [14–16].

The issue of analyzing the indentation data in the sense of identifying the material parameters of a viscoplastic constitutive model has been treated in a series of recent publications [17–20]. Based on a simple empirical model a new loading history as shown in Fig. 2 was proposed in [17]. It allows for separating the rate independent (plastic) part of the indentation loading response from the time/rate dependent (viscous) part by introducing three intermediate creep phases c1–c3, each of 100 s at equidistant force intervals. A final creep phase c4 at maximum load and of 600 s duration provides the necessary data for the identification of the viscosity parameters. Viscous processes, which are responsible for a more or less rate sensitive material response, can be observed in all types of metals deformed beyond their yield stress at a given positive loading rate. After loading, the induced viscous overstress is reduced by a time dependent material deformation during fixed load or displacement. This effect causes even at room temperature a time dependent deformation behavior within the specimen until an equilibrium has been reached. Such phenomena are classified in general mechanics as creep and relaxation. It should be noted that classical creep as it is known in materials science is a special case that is only observed at higher temperatures. Nevertheless, a so-called 'creep phase' can be observed in an indentation experiment at room temperature that represents a time dependent deformation process at constant load, which rapidly decreases in velocity and allows identifying the rate dependent (viscous) portion of the total stress.

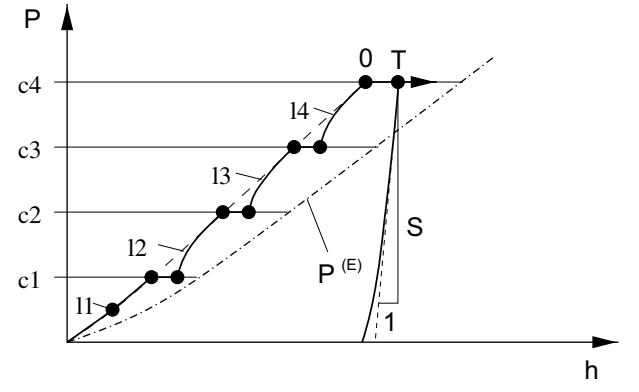

Fig. 2. Loading history for identification of material parameters in a viscoplasticity model.

An important quantity that is directly correlated to the reduced modulus $E_r := E/(1-\nu^2)$ of the material is the unloading stiffness S [4]. From a subsequent unloading–reloading cycle the modulus and the kinematic hardening of the material can be determined, while the equilibrium stress–strain behavior corresponding to the equilibrium loading response $P^{(E)}(h)$ is derived from the loading response in combination with the end points of the intermediate creep phases [18]. An experimental validation of the method is presented in [19] using a Zwick hardness tester (Zwick/Roell), with tip radii of 200–500 μm on a variety of materials, but restricted to the assumption of pure isotropic hardening. A further validation extended by a geometry correction for typically imperfect spherical indenters of 2–10 μm radius used in a nanoindentation device has been conducted in [20], where it has been shown that the identified viscoplastic model predicts the independently measured rate dependent tensile behavior of nanocrystalline nickel [21] extremely well.

By combining a Zwick hardness tester, modified for remote controlled use in a Hot Cell, with the developed neural network analysis software a new indentation system is provided that allows for performing important tests on irradiated materials. In this paper also the identification module for kinematic hardening [18] is presented for the first time in an application to experimental data from indents on Eurofer 97. Due to the depth measurement principle of most indentation systems this technique is very sensitive to temperature drift so that all experiments are currently restricted to room temperature. The constitutive model and the neural network software however allow the identification of time dependent behavior and the approach can be used in the very same way for the analysis of experimental data measured at higher temperatures. It is therefore planned to extend the current experimental setup by a high-temperature indentation system.

2. Experimental details

For the specification of the indentation device a series of preliminary experiments have been carried out using an existing Zwick hardness tester [19]. Goal was a maximum force and depth resolution and measurement accuracy in the force range required for the materials under consideration. Due to its high hardness tungsten defines the maximum force at a given ratio of depth to indenter radius $h/R = 0.1$ that is required for the application of the neural networks. Motivated by the limited amount of material in dimension of a few millimeters, two indenter radii of 200 μm and 500 μm,

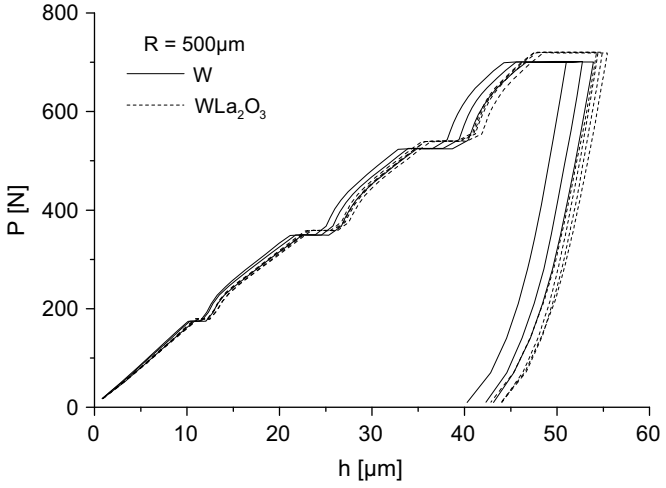

Fig. 3. Force–depth behavior for bulk W and WLa_2O_3 measured with a 2.5 kN hardness measurement head.

Table 1
Maximum force necessary for spherical indentation at $R = 250$ μm

Material, behavior at room temperature	Eurofer 97 EA33, ductile	MANET-II EM19, ductile	MANET-II EM11, brittle	W, brittle	W-La_2O_3, brittle
Austenized at	980 °C	1075 °C	1075 °C		
Annealed at	760 °C	700 °C	600 °C		
$R_{p0.2}$	537 MPa	736 MPa	869 MPa		
R_m	652 MPa	839 MPa	973 MPa		
Force at $h/R = 0.1$	83 N	100 N	118 N	175 N	180 N

respectively, were considered. The two hardness measurement heads supplied by Zwick/Roell provide a maximum application force of 200 N and 2500 N, respectively. As it can be seen in Fig. 3, the 500 μm tip requires only about a third of the larger load cell for bulk tungsten and WLa_2O_3. By scaling this force down to 200 μm radius by $P/R^2 = \text{const}$, which corresponds to a standard Rockwell indenter, a maximum load of about 110 N results, which uses a major part of the force range of the smaller measurement head with sufficient distance to the maximum force.

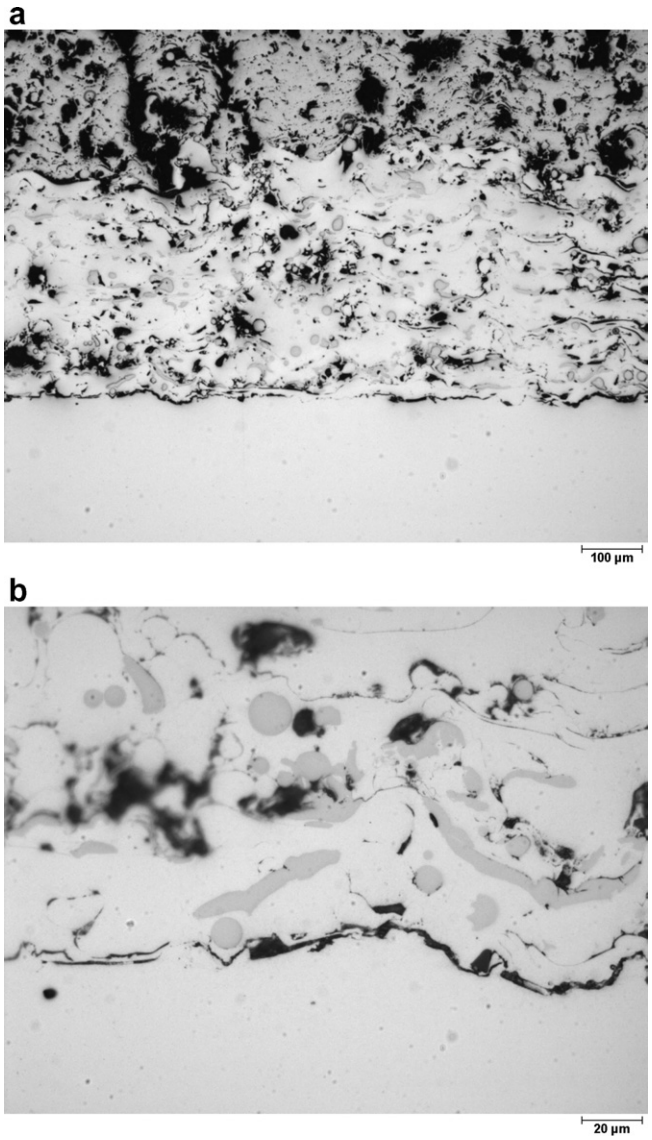

Fig. 4. Micrographs of a plasma sprayed W-coating on Eurofer: (a) scale 100 μm; (b) scale 20 μm.

Table 1 summarizes the maximum forces for fusion relevant alloys determined with a slightly larger indenter radius of $R = 250$ μm.

Also for this indenter, all materials are covered by the smaller hardness measurement head resulting in an optimal measurement accuracy and resolution. To enhance the accuracy in the depth resolution, the version with the higher depth resolution of 20 nm was chosen. Special control software was provided by Zwick/Roell as an extension to the standard TestXpert software, which allows performing the more general loading history, sketched in Fig. 2 including load cycles and different hold segments.

To ensure a proper functionality and reliability under radiating environment a variety of modifications has been included, like a special varnishing that allows the decontamination before inspection and repair, a radiation-resistant damping system to insulate the machine against vibrations transmitted by the Hot Cells' structure, a shielding of the electronics in the hardness measurement head by a thick steel base and the location of the control box outside of the Hot Cell. The machine has a remote controlled x–y stage and a microscope for remote positioning of the specimen as well as a special tip holder that allows a fast exchange with manipulators.

Due to the reduction of the tip radius to 200 μm, the maximum indentation depth is about 20 μm. The thickness of W-coatings currently under discussion is about 2.5 mm and the ratio of maximum indentation depth to coating thickness is by far less than 10%. Under such conditions the influence of the substrate can be neglected and the analysis can assume a bulk material. In Fig. 4 micrographs of a plasma sprayed W-coating on top of an Eurofer substrate are presented. It can be seen that the W-coating consists of two layers, a thinner one with a thickness of about 1 mm is next to the substrate. The W-coating is rich of large pores with diameters from 10 μm to 200 μm. To carry out indentation experiments, the specimen was carefully polished and only good areas were used for indents. This underlines the requirement that the indenter must be equipped with a calibrated optical microscope and a remote controlled x–y-stage to choose appropriate places for the indents.

3. Computational methods

3.1. Constitutive model

The constitutive model has been selected because it is able to describe the elastic–viscoplastic behavior of metals, such as those which are relevant for first wall fusion applications. We use a Chaboche like unified viscoplastic material model with a distinct elastic range, a rate independent nonlinear isotropic and kinematic hardening of Armstrong–Frederick type and a rate dependent viscous overstress. Compared to frequent used power-law type hardening models this unified constitutive model has several advantages (see also [22]):

- It describes the hardening behavior of a wide range of materials very well,
- the material response for more complex loading histories, e.g. including cyclic loading, dwell-times and time dependent loading rate, can be predicted,
- the same model can be used over a wide range of temperatures using temperature dependent material parameters with the possibility of describing changing phenomena over temperature without changing the model, and
- it is possible to easily interpolate the material parameters over temperature in a physically meaningful way.

This model contains some assumptions, such as saturation in the Armstrong–Frederick type hardening rules. The work of Spätig

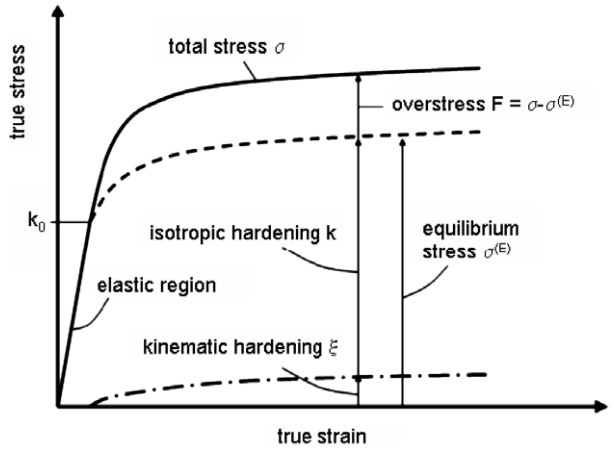

Fig. 5. Response for tensile loading with the rate dependent plasticity model.

(see e.g. [23]), who has successfully used this type of hardening rule in form of Eq. (2) for the finite element simulation of small punch tests, has shown that this assumption is suitable to describe the measured hardening behavior of irradiated materials.

The model is formulated based on large deformation theory and has been implemented by [24] as a user material (UMAT) in ABAQUS. For a better understanding, the properties of the model are discussed for the case of small deformations, yielding the following set of constitutive equations:

$$
\begin{aligned}
&\varepsilon = \varepsilon_{\mathrm{e}} + \varepsilon_{\mathrm{i}} \\
&\sigma = E\varepsilon_{\mathrm{e}} \\
&\dot{\varepsilon}_{\mathrm{i}} = \frac{\langle F \rangle^{m}}{\eta} \\
&F = \mid \sigma - \xi \mid - k(= (\eta\dot{\varepsilon}_{\mathrm{i}})^{1/m}) \\
&k = k_0 + \frac{\gamma}{\beta}(1 - \mathrm{e}^{-\beta s}) \\
&\dot{\xi} = \frac{3}{2}c\dot{\varepsilon}_{\mathrm{i}} - b\dot{s}\xi \\
&s = \int_{\tau=0}^{t} \mid \dot{\varepsilon}_{\mathrm{i}}(\tau) \mid \mathrm{d}\tau.
\end{aligned}
\tag{1}
$$

In this set of equations ε, ε_{e}, and ε_{i} denote the total strain, elastic strain, and the inelastic strain, respectively. As shown in Fig. 5, the stress σ is given by Hook's law with Young's modulus E and depends on additional internal variables, which are the overstress F, the isotropic hardening k, and the kinematic hardening ξ. The result of the operator $\langle F \rangle$ is $\langle F \rangle = F$ for $F > 0$ (viscoplastic loading), and $\langle F \rangle = 0$ (elastic loading/unloading) otherwise. Fig. 5 shows the typical response of the assumed material law under tensile loading at constant strain rate.

The viscosity exponent m is responsible to describe the rate sensitivity of the overstress, which can be expressed in terms of two different inelastic strain rates $F_1/F_2 = \sqrt[m]{\dot{\varepsilon}_{\mathrm{i}1}/\dot{\varepsilon}_{\mathrm{i}2}}$, i.e. the strain rate sensitivity decreases with increasing viscosity exponent m. The viscosity parameter η defines in connection with the viscosity exponent m the amount of overstress at a given strain rate. Because η has a unit that depends on the value of the viscosity parameter m, it is convenient to make use of the initial overstress at the beginning of the last creep segment F_0, which has a stress unit and thus can be easily compared with the yield stress k_0 or the total stress σ. Note that the initial overstress F_0 depends besides m and η also on the force application rate and is therefore not a real material parameter. However, it is a good measure for the contribution of viscosity to the total stress.

The accumulated plastic strain s is responsible for the evolution of the isotropic hardening k, which is determined by the yield stress k_0, the initial slope of work hardening γ, and the work hardening parameter β. Similarly, the initial slope of kinematic hardening is defined by $1.5c$ while the parameter combination $1.5c/b$ determines the upper bound of kinematic hardening.

For a better interpretation of the hardening parameters, an additional parameter Σ, which is the total hardening for $s \to \infty$ in tensile loading, is introduced by $\Sigma := k_0 + \gamma/\beta + 1.5c/b$. This parameter represents the equilibrium stress at infinite plastic strain and limits the total hardening behavior such that $k_0 \leqslant \xi + k \leqslant \Sigma$. More details on the interpretation of the model in Eq. (1) are given elsewhere [22].

3.2. Neural network analysis

The identification method based on neural networks has been described in detail elsewhere [18,19] and will be summarized in this section. The neural network software used in this work has been implemented as an additional analysis module into the IndentAnalyser software available from ASMEC (Germany). In order to determine all three different contributions, k, ξ, and F to the total stress–strain behavior uniquely, the loading history with multiple creep segments during loading has been applied [17]. For identifying the kinematic hardening behavior $\xi(s)$, an unloading–reloading cycle at the maximum force is required.

The indentation tests are performed using a multi-creep loading history consisting of three creep segments at the forces $0.25P_0$, $0.5P_0$, and $0.75P_0$ of 100 s duration and one period of creep at the maximum force P_0 of 600 s. The three creep segments during the loading process are required in order to achieve a higher accuracy in the equilibrium response and viscosity parameters. Since the neural networks were trained for selected ranges of the test conditions, the maximum force P_0 has to be chosen in order to achieve an indentation depth h_0, which is the depth at the end of the last loading segment, between 8% and 12% of the nominal indenter radius R. The range of the force application rate is determined by the time h_0 within 10–60 s, which is defined as the time for loading without the periods of creep. The unloading rate has to be equal to the force application rate.

In order to limit the number of neurons and the training time of neural networks, the experimental data used for the input into the neural networks have to be selected carefully. For that reason, the data were discretized in 10 equidistant increments for each segment (see [18,19] for more details). All neural networks are trained with dimensionless data and, as far as possible, prior knowledge has been included in order to achieve a maximum generality. The first neural network, denoted by ZeroNet performs the zero point correction h_z in the depth data, limited to an interval of $-5 \times 10^{-3} \leqslant h_z/R \leqslant 5 \times 10^{-3}$. The identification of Young's modulus using ENet follows from the information given by the maximum depth at the end of the last creep segment h_{T}, unloading stiffness S and the form of loading curve given by ratios of forces at defined indentation depths. The viscosity parameter η is calculated from the values of F_0 and m, which are determined from data of the loading, creep phases and the unloading stiffness using ViscNet. From the same data the equilibrium stress–strain curve $\sigma^{(\mathrm{E})}(\varepsilon_{\mathrm{i}})$ is determined at the true plastic strains $\varepsilon_{\mathrm{i}} = \{0, 0.01, 0.02, 0.04, 0.08, 0.16, 0.32\}$ by SigmaNet. The determination of the kinematic hardening rule $\xi(s)$ is optionally performed using additional data from the unloading–reloading hysteresis by XiNet, which splits the equilibrium stress–strain response in its two parts $\sigma^{(\mathrm{E})}(\varepsilon_{\mathrm{i}}) = k(\varepsilon_{\mathrm{i}}) + \xi(\varepsilon_{\mathrm{i}})$. By fitting the identified stress–strain data points with the following equations derived from Eq. (1) for monotonic tensile loading

$$k(\varepsilon_i) = k_0 + \frac{\gamma}{\beta}(1 - \exp(-\beta\varepsilon_i)), \quad (2)$$

and

$$\xi(\varepsilon_i) = \frac{3}{2}\frac{c}{b}(1 - \exp(-b\varepsilon_i)), \quad (3)$$

the material parameters k_0, γ, β and c, b are determined, respectively. If only isotropic hardening is assumed, the parameters for the isotropic hardening rule k_0, γ, and β are determined by fitting Eq. (2) to $\sigma^{(E)}(\varepsilon_i)$ while the material parameters c and b are set to zero.

4. Results and discussion

4.1. Eurofer 97

A series of reference indentation tests has been performed before starting the necessary modifications in the mock-up, where the performance of remote controlled setup is being tested. The measured data for Eurofer 97, discretized conveniently for calculating the neural network inputs, are plotted in Fig. 6. Eurofer 97 has been chosen as a reference material and it can be seen from the small scatter in Fig. 6 that (i) this material is very homogeneous and (ii) that the indentation device has a very good repeatability. The deviation of Eurofer 3 and 4 from the other experiments is due to thermal drift that can cause an artificial negative creep and vanishes as soon as the specimen reaches the temperature of the machine. From experiment Eurofer 5 and higher, there is almost no deviation visible between the experiments. Therefore the experiments Eurofer 3 and 4 have been excluded from the following analysis. Note that the effect of reverse plasticity, which is due to kinematic hardening and similar for all experiments, can be seen nicely for the shifted unloading–reloading curve of experiment Eurofer 3.

The identification method described in Section 3 has been applied to the data shown in Fig. 6. Eight material parameters (Young's modulus and yield strength, two hardening parameters for each hardening rule as well as two viscosity parameters) can be identified within a few milliseconds. The material parameters can be used to simulate the stress–strain behavior of the tested material for any loading history as well as for dimensioning of parts using finite element simulations. Since the parameters describing kinematic hardening are determined in the last step, they are afflicted with the highest identification uncertainties. Depending on the quality of the specimen and the experiment, it can happen that only the total hardening behavior can be determined.

The machine compliance is a parameter, which has to be provided to the analysis software, has been adjusted to $C_m = 8.5 \times 10^{-6}$ mm/N to obtain the correct Young's modulus for Eurofer. The scatter of all determined values of E is within 4 GPa, which is less than 2%. For this material both options (identification of pure isotropic hardening as well as isotropic and kinematic hardening) have been applied so that slightly different results are obtained from the same experiments. The results are presented in Fig. 7 in comparison with data from a tensile experiment [25]. Both cases show a very good agreement between tensile and indentation data. It can be seen that by including kinematic hardening the nonlinearity of the stress–strain behavior at the onset of plastic deformation and at ultimate tensile strength is described slightly better. The identified contribution of kinematic hardening, which is important for cyclic loading of a material, is significant as shown in Fig. 8. The observed scatter can be attributed to a major part to the initial slope of the identified kinematic hardening rule while the asymptotic value is very stable for all experiments.

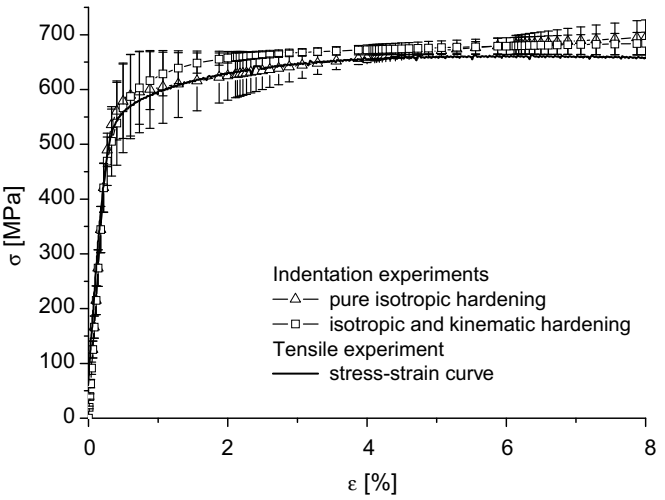

Fig. 7. Identification of stress–strain behavior for Eurofer 97 under the assumption of pure isotropic hardening as well as isotropic and kinematic hardening.

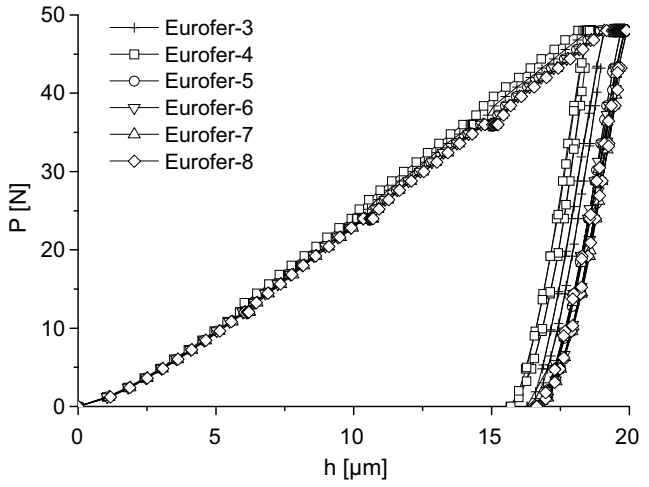

Fig. 6. Indentation experiments with Zwick-Indenter for Eurofer 97 (EA33).

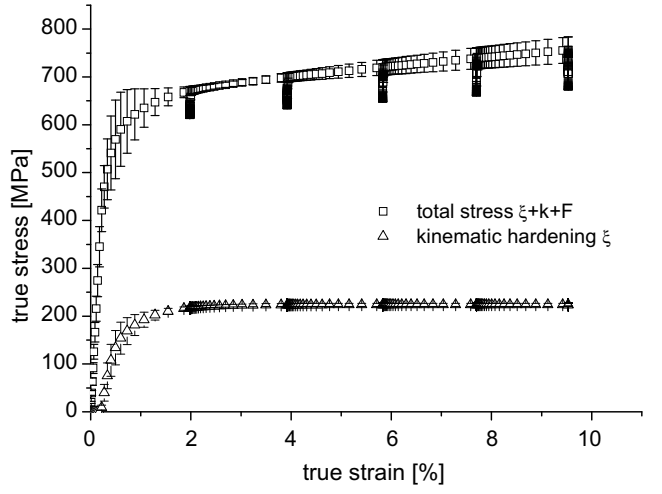

Fig. 8. Contribution of kinematic hardening to the total hardening response of Eurofer 97 in a true stress–true strain diagram.

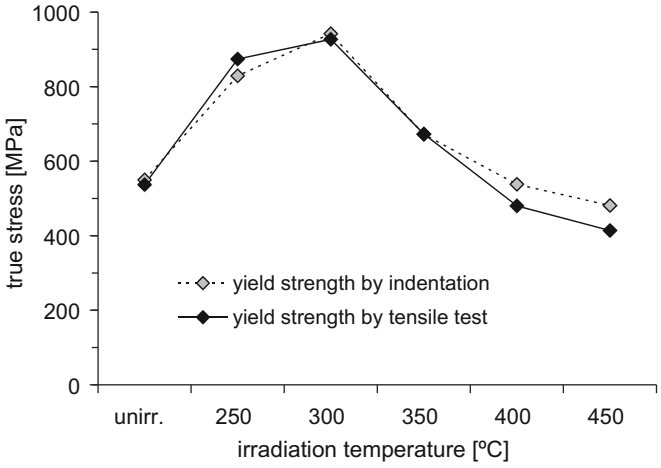

Fig. 9. Yield strength of 15 dpa-irradiated Eurofer 97, determined by tensile experiments (full lines) and by instrumented indentation (dotted lines).

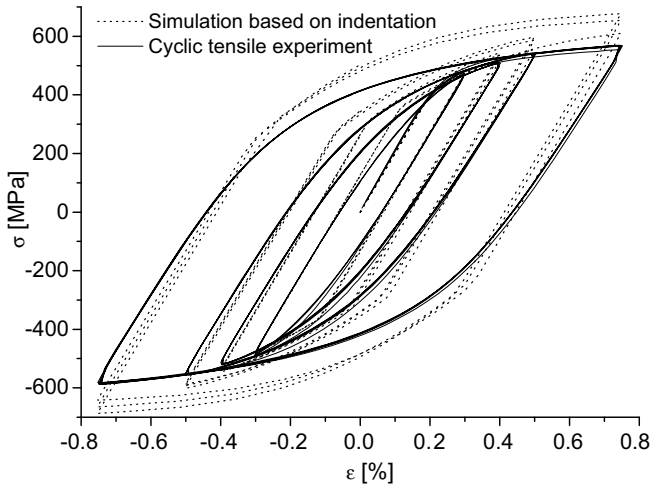

Fig. 10. Stress–strain behavior of Eurofer under cyclic loading with different strain rates. Full lines represent experiments, dotted lines are simulations based on indentation experiments.

Using this approach, stress–strain curves were identified for Eurofer 97 after irradiation at different temperatures. The irradiation was done in the Petten High Flux Reactor at temperatures of 250, 300, 350, 400, and 450 °C up to a damage dose rate of 15 dpa in steel. Material properties, such as the yield stress, are obtained as well by instrumented indentation, as by conventional tensile experiments with round tensile specimens of $18 \times \varnothing 3$ mm^2 [26]. The material exhibits clear embrittlement and hardening after irradiation. Embrittlement depends on the irradiation temperature and is and worse for lower irradiation temperatures. The according strong changes in yield strength can be determined by both methods, tensile and indentation test, in good accordance. The differences in yield strength for the higher irradiation temperatures are due to the fact that tensile tests are carried out at irradiation temperature, but indentation experiments only can be done at room temperature so far. However, it is shown that even the exceptional behavior of steel irradiated up to a considerable damage dose rate can be identified by the neural networks analysis (see Fig. 9).

Fig. 10 shows the applicability of this method to cyclic experiments, performed on Eurofer specimens with a different geometry from the pure tensile tests. The cyclic experiments that have been carried out at 0.25 Hz and different strain amplitudes of 0.15, 0.20, 0.50, and 0.75% are represented by full lines. The material parameters for modulus, viscosity, and isotropic and kinematic hardening, identified from the indentation experiments described above, supply the calculated curves (dotted lines) by numerical integration of the model in Eq. (1) with the given cyclic loading history and strain rates of the experiments. Clearly the material model can not describe Eurofer's cyclic softening behavior, but we find an excellent agreement between experiments and prediction for the first few cycles at different strain amplitudes. It should be noted that no curve fitting has been carried out and the remaining deviations between the experimental and predicted behavior is caused by identification uncertainties in the neural network approach. In particular the very same saturation behavior of the isotropic hardening is correctly reflected in Fig. 10 in form of the stabilization of the cyclic stress–strain hysteresis loop. Further, the good agreement of the hysteresis loops predicted for different strain amplitudes indicate that the assumption of an Armstrong–Frederick type kinematic hardening rule with its distinct saturation behavior is appropriate to describe the cyclic material behavior of Eurofer 97.

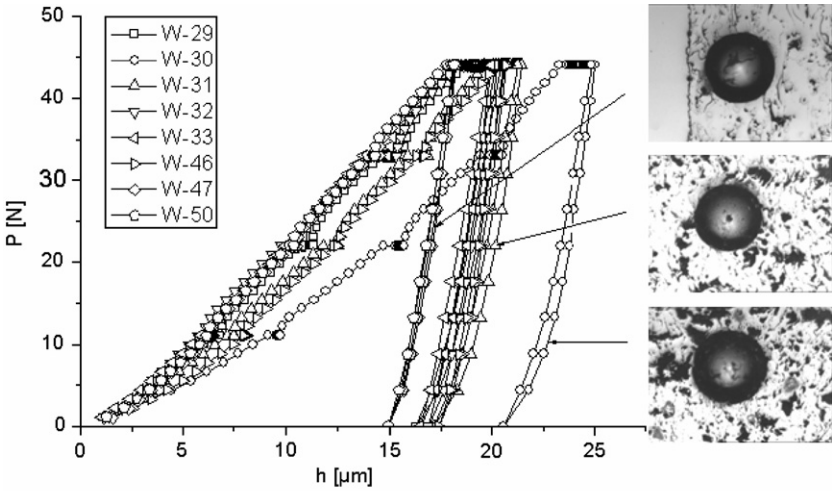

Fig. 11. Force–depth curves for a W-coating deposited on Eurofer. The interface between tungsten and Eurofer 97 can be seen in the upper right micrograph.

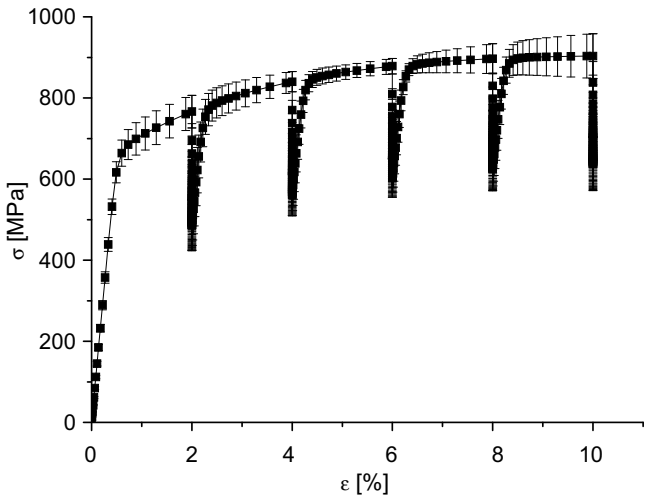

Fig. 12. Stress–strain behavior with inserted relaxation phases of 3600 s for a plasma sprayed tungsten coating of 2 mm thickness.

4.2. Tungsten coatings

The applicability of the whole method for tungsten coatings is demonstrated with indents made in a cross-section of a polished W-coating deposited on a substrate made of Eurofer 97. The micrographs in Fig. 11 indicate possible difficulties with indenting the W-coating. The indent should have sufficient distance to the interface (upper micrograph) and should not be positioned in the vicinity of big pores (lower micrograph), which are typical for the plasma deposited coating. The lines connect inapplicable positions with the resulting force–depth curves, which show large deviations from those obtained at better locations. The height of the coating is about 2 mm and therefore sufficient material is available for the about 100 μm wide imprints, which can be identified using the positioning system before the experiment. The middle micrograph shows such an indent in a typical area for which the most reproducible results have been obtained.

The stress–strain behavior identified by the analysis software from experiments W-31–33 is presented in Fig. 12. For the other experiments, the bad positioning of the indent leaded to significant misinterpretation of the deformation behavior by the neural networks.

The obtained stress–strain behavior for the tungsten coating shows a much 'softer' behavior than that of bulk tungsten. Using the relationship between elastic modulus and porosity of Kupkova [27], we can estimate from the measured and the bulk moduli, which are 130 GPa and 411 GPa, respectively, a porosity of the coating between 27% and 46%. This large porosity is confirmed by the micrographs in Figs. 4 and 11. A significant viscous overstress is visible from the inserted relaxation phases. The identified yield strength is 390 ± 81 MPa and the maximum equilibrium strength of the coating material is 645 ± 130 MPa. At a strain rate of $\dot{\varepsilon} = 10^{-3}\ s^{-1}$ the estimated ultimate tensile strength is about 900 MPa.

It is clear, that the high content of large pores does not allow interpreting these data in the same way as an average response from a macroscopic tensile test. Compared to a hardness test it is however possible to obtain some additional useful information on the mechanical behavior, which can be investigated as a function of the irradiation temperature and dose rate. In this way, small amounts of material can be efficiently characterized with this technique in order to provide important information for the further process optimization.

5. Conclusions

The results show the feasibility and the potential of an indentation device for highly radioactive materials in the Fusion Materials Laboratory (FML). Brittle materials like bulk tungsten and tungsten coatings can be tested easily with indentation methods. Compared to other existing techniques, such as the ABI-technique, which are limited to power-law hardening and simple tension, rich information on the mechanical properties, like e.g. Young's modulus, true stress–strain curve, cyclic behavior, and time dependent behavior can be obtained before and after irradiation with high accuracy. This additional information in form of material parameters for a unified viscoplastic constitutive model allows further to predict the deformation behavior of complex structures and loading histories using the finite element method.

The approach has also been applied to tungsten coatings, which cannot be characterized by tensile experiments due to their brittleness. The results show a significant scatter of the determined stress–strain behavior due to the presence of large pores in the coatings. The approach is however very useful for investigation of such difficult materials in order to evaluate at least the qualitative effect of irradiation on mechanical properties of interest.

Acknowledgements

This work was partially funded by German Research Foundation (DFG) Grants Hu 844/1-1 and Hu 844/1-2 and by EFDA within the task TW4-TTMA-002-D3. We would also like to thank Christian Ullner BAM Berlin for his very helpful suggestions and his support with preparatory experiments as well as FZK and ASMEC Germany for financial support and implementation of the neural network identification software in a user friendly graphical user interface, respectively, within the technology transfer project TT-U041.

References

[1] A. Möslang, E. Diegele, M. Klimiankou, R. Lässer, R. Lindau, E. Lucon, E. Materna-Morris, C. Petersen, R. Pippan, J.W. Rensman, M. Rieth, B. van der Schaaf, H.-C. Schneider, F. Tavassoli, Nucl. Fusion 45 (2005) 649.
[2] E. Gaganidze, H.-C. Schneider, B. Dafferner, J. Aktaa, J. Nucl. Mater. 367–370 (2007) 81.
[3] C. Petersen, A. Povstyanko, V. Prokhorov, A. Fedoseev, O. Makarov, B. Dafferner, J. Nucl. Mater. 367—370 (2007) 544.
[4] W.C. Oliver, G.M. Pharr, J. Mater. Res. 7 (1992) 1564.
[5] T. Yamamoto, H. Kurishita, T. Matsushima, H. Kayano, J. Nucl. Mater. 239 (1996) 219.
[6] F.M. Haggag, In situ measurements of mechanical properties using novel automated ball indentation system, ASTM STP 1204, 1993, p. 27.
[7] T. Yamamoto, H. Kurishita, H. Matsui, J. Nucl. Mater. 271&272 (1999) 440.
[8] Y. Katoh, H. Tanigawa, T. Muroga, T. Iwai, A. Kohyama, J. Nucl. Mater. 271 (1999) 115.
[9] M. Ando, H. Tanigawa, S. Jitsukawa, T. Sawai, Y. Katoh, A. Kohyama, K. Nakamura, H. Takeuchi, J. Nucl. Mater. 307 (2002) 260.
[10] N. Sekimura, T. Kamada, Y. Wakasugi, T. Okita, Y. Arai, J. Nucl. Mater. 307 (2002) 308.
[11] Y. Katoh, M. Ando, A. Kohyama, J. Nucl. Mater. 323 (2003) 251.
[12] T.S. Byun, S.H. Kim, B.S. Lee, I.S. Kim, J.H. Hong, J. Nucl. Mater. 277 (2000) 263.
[13] B. Taljat, G.M. Pharr, Int. J. Solids Struct. 41 (2004) 3891.
[14] J.-H. Ahn, D. Kwon, J. Mater. Res. 16 (2001) 3170.
[15] S. Kucharski, Z. Mróz, J. Eng. Mater. Tech. 123 (2001) 245.
[16] A. Nayebi, R. El Abdi, O. Bartier, G. Mauvoisin, Mech. Mater. 34 (2002) 243.
[17] N. Huber, E. Tyulyukovskiy, J. Mater. Res. 19 (2004) 101.
[18] E. Tyulyukovskiy, N. Huber, J. Mater. Res. 21 (2006) 664.
[19] D. Klötzer, Ch. Ullner, E. Tyulyukovskiy, N. Huber, J. Mater. Res. 21 (2006) 677.
[20] E. Tyulyukovskiy, N. Huber, J. Mech. Phys. Solids 55 (2007) 391.
[21] R. Schwaiger, B. Moser, M. Dao, N. Chollacoop, S. Suresh, Acta Mater. 51 (2003) 5159.
[22] N. Huber, Ch. Tsakmakis, Comput. Meth. Appl. Mech. Eng. 191 (2001) 353.
[23] G.E. Lucas, G.R. Odette, H. Matsui, A. Möslang, P. Spätig, J. Rensman, T. Yamamoto, J. Nucl. Mater. 367–370 (2007) 1549.
[24] E. Diegele, W. Jansohn, Ch. Tsakmakis, Comput. Mech. 25 (2000) 1.
[25] H.C. Schneider, Development of a miniaturized fracture mechanics specimen for post-irradiation testing (in German), Scientific Report, FZKA-7066 (September 2005) and Dissertation, Universität Karlsruhe, 2005.
[26] C.E. Materna-Morris, A. Möslang, R. Rolli, H.-C. Schneider, J. Nucl. Mater., in press.
[27] M. Kupkova, J. Mater. Sci. 28 (1993) 5265.